water

MDPI

Article

Evaluation of the Sensitivity of the Weather Research and Forecasting Model to Changes in Physical Parameterizations During a Torrential Precipitation Event of the El Niño Costero 2017 in Peru

Alejandro Sánchez Oliva [1], Matilde García-Valdecasas Ojeda [1,2,*] and Raúl Arasa Agudo [3]

[1] Departamento de Física Aplicada, Universidad de Granada, 18071 Granada, Spain; alex102010so@gmail.com
[2] Instituto Interuniversitario de Investigación del Sistema Tierra en Andalucía (IISTA-CEAMA), 18071 Granada, Spain
[3] Applied Research, Meteosim, 08028 Barcelona, Spain; rarasa@meteosim.com or rarasaag@gmail.com
* Correspondence: mgvaldecasas@ugr.es

Abstract: This study evaluates the sensitivity of the Weather Research and Forecasting (WRF-ARW) model in its version 4.3.3 during different experiments on a torrential precipitation event associated with the 2017 El Niño Costero in Peru. The results are compared with two reference datasets: precipitation estimations from CHIRPS satellite data and SENAMHI meteorological station values. The event, which had significant economic and social impacts, is simulated using two nested domains with resolutions of 9 km (d01) and 3 km (d02). A total of 22 experiments are conducted, resulting from the combination of two planetary boundary layer (PBL) schemes: Yonsei University (YSU) and Mellor–Yamada–Janjic (MYJ), with five cumulus parameterization schemes: Betts–Miller–Janjic (BMJ), Grell–Devenyi (GD), Grell–Freitas (GF), Kain–Fritsch (KF), and New Tiedtke (NT). Additionally, the effect of turning off cumulus parameterization in the inner domain (d02) or in both (d01 and d02) is explored. The results show that the YSU scheme generally provides better results than the MYJ scheme in detecting the precipitation patterns observed during the event. Furthermore, it is concluded that turning off cumulus parameterization in both domains produces satisfactory results for certain regions when it is combined with the YSU PBL scheme. However, the KF cumulus parameterization is considered the most effective for intense precipitation events in this region, although it tends to overestimate precipitation in high mountain areas. In contrast, for lighter rains, combinations of the YSU PBL scheme with the GD or NT parameterization show a superior performance. It is worth nothing that for all experiments here used, there is a clear underestimation in terms of precipitation, except in high mountain regions, where the model tends to overestimate rainfall.

Keywords: precipitation events; Weather Research and Forecasting; El Niño Costero; sensitivity analysis; physics schemes; Peru

Academic Editor: Paul Kucera

Received: 2 December 2024
Revised: 3 January 2025
Accepted: 8 January 2025
Published: 14 January 2025

Citation: Oliva, A.S.; García-Valdecasas Ojeda, M.; Arasa Agudo, R. Evaluation of the Sensitivity of the Weather Research and Forecasting Model to Changes in Physical Parameterizations During a Torrential Precipitation Event of the El Niño Costero 2017 in Peru. *Water* **2025**, *17*, 209. https://doi.org/10.3390/w17020209

1. Introduction

The coast of Peru is characterized by scarce precipitation due to three main factors: (1) **the presence of trade winds and southeasterly winds**, influenced by the South Pacific Anticyclone, which bring colder and denser air to the tropical region; (2) **coastal upwelling**, which leads to cold sea surface temperatures (SSTs); and (3) **the presence of the Cordillera Blanca**, a mountain range that is part of the Andes running through Peru, generating

subsidence to the west, on the leeward side [1]. These three factors create a stable situation that favors a strong thermal inversion, inhibiting convection.

However, extreme or torrential precipitation events occur cyclically in Peru, mainly driven by the El Niño-Southern Oscillation (ENSO) [2]. The ENSO is one of the most globally influential climate patterns and is the dominant mode of coupled atmosphere–ocean variability on interannual time scales [3].

The warm phase of the ENSO, known as El Niño, can cause, among many other things, an increase in temperature by several degrees Celsius above normal in the Pacific Ocean, a weakening of the trade winds or even their reversal, as well as a deepening of the thermocline [4]. This results in strong convection, further intensified by the increased moisture in the atmosphere due to the warming of the Pacific Ocean, leading to episodes of extreme and prolonged rainfall. In the cold phase of the ENSO, La Niña, the trade winds strengthen, resulting in an increase in their intensity [5]. This causes a decrease in SST due to the upwelling of cold waters along the Peruvian coast, reducing convection and creating colder and drier than usual conditions in the region.

To determine whether the current ENSO phase is cold, warm, or neutral, a variety of indices based on different climate variables have been developed: the Southern Oscillation Index (SOI), which is based on sea level pressure (SLP), and the Oceanic Niño Index (ONI) and the El Niño Costero Index (ICEN), both based on SST values. For the latter, the Pacific Ocean is divided into regions. The ONI corresponds to the SST anomaly calculated as a 3-month moving average in region 3.4 (from 5° N–5° S of latitude and 120° W–170° W of longitude). It is calculated with reference to a 30-year average and reflects large-scale conditions most representative of the central Pacific [6]. On the other hand, ICEN is the index used by the Multisectoral Commission for the Study of the El Niño Phenomenon (ENFEN) to monitor El Niño and La Niña along the Peruvian coast, specifically in the Niño 1 + 2 region (10° S–0° S of longitude and 90° W–80° W of latitude). For this region, the index corresponds to the SST anomaly with reference to the 1981–2010 period. The importance of the ICEN lies in the fact that, in the last 100 years, there have been five anomalous warming events in the eastern Pacific Ocean waters (region 1 + 2), i.e., along the coasts of Peru and Ecuador, while the waters of the central Pacific (region 3.4) have remained at normal temperatures. These events, with warm conditions in the eastern Pacific but neutral or cold conditions in the central Pacific, are referred to as El Niño Costero (ENC) [7].

The origin of El Niño Costero remains a subject of debate. On the one hand, Takahashi and Martínez [8] argued that coupled ocean–atmosphere processes, linked to the strengthening of the southern band of the Intertropical Convergence Zone (ITCZ), are the main mechanisms responsible for the weakening and detachment of the southern trade winds in January. On the other hand, Garreaud [7] suggests that atmospheric forcing through the weakening of the westerly winds flowing over the subtropical Andes is directly related to these events.

In 2017, there was an El Niño Costero event, which was considered “moderate”. The anomalous warming of the sea along the Peruvian coast triggered heavy torrential rains that affected the entire country; they were highly destructive, causing overflows, floods, and landslides. During the months that El Niño Costero lasted, more than 1.9 million people were affected, resulting in 162 deaths and billions of euros in material losses [9,10]. This does not include those affected by subsequent diseases caused by the floods, such as dengue. The great impact of the 2017 El Niño Costero makes the disaster comparable to the floods caused by El Niño itself in 1982–1983 and 1997–1998, which were classified as very strong.

Given the value and importance of predicting ocean–atmosphere processes, progress in the evaluation and verification of numerical models that provide these forecasts is

necessary [11]. A numerical model used by the scientific community to predict these types of extreme or torrential phenomena is Weather Research and Forecasting (WRF) [12].

The WRF model is a next-generation numerical computation system used for both research and weather forecasting [12], as well as regional climate research [13–15]. This model provides a large variety of parameterizations, which are simplified representations of physical processes occurring at scales smaller than the model's resolution. These parameterizations are critical since they define the model's accuracy across diverse climate conditions and geographical regions. Therefore, the selection of an appropriate combination of parameterizations is crucial to improving the reliability of predictions, especially in complex events such as those associated with El Niño Costero.

In South America, the use of WRF as a research and forecasting model is booming [16]. For instance, studies such as that by Müller et al. [17] found WRF to be an accurate tool to produce continent-wide forecasts at a spatial resolution of 45 km and using a 15 km nested domain of up to 7 days. On the other hand, a study conducted with WRF at 25 km of spatial resolution over northern South America and the Caribbean Sea from 1982 to 2012 [18] concluded that positive biases in precipitation were due to poor representations of regional flows and corresponding effects on convergence zones, as well as poor representations of Pacific SSTs. These results align with those proposed by Back and Bretherton [19].

Specifically for our study area, Ordoñez Piscoya [20] analyzed the model's sensitivity for northern Peru using a configuration based on two domains (one with a 9 km resolution and the other nested at a 3 km spatial resolution) and testing two convection schemes (CU), Kain–Fritsch (KF) and Grell–Freitas (GF), as well as through the explicit resolution of this phenomenon. The results showed that for the 3 km spatial resolution domain, the most suitable configurations were those using the GF convection scheme. However, at a 9 km resolution, KF-based configurations gave better results, although in both cases, precipitation was overestimated.

In another study over the southeast of Peru [16], the KF and GF cumulus parameterization schemes were compared with the YSU planetary boundary layer (PBL) scheme. González-Rojí et al. found that GF overestimated precipitation values, although they recommended it over the KF scheme, which significantly underestimated accumulated precipitation. Similarly, Uribe [21] investigated WRF's ability to simulate extreme precipitation values, in this case using only the KF cumulus parameterization, concluding that this scheme has limited ability to simulate extreme events as it underestimates precipitation. Another simulations over the Andes and western slopes with the same radiation and microphysics schemes considered in this work [22], in addition to the YSU parameterization for PBL and the Grell–Devenyi (GD) cumulus parameterization, found that the complexity of the area due to topography and precipitation gradients makes spatial resolutions of 9 km insufficient to capture the quantities and patterns of precipitation over the Cordillera Blanca. A different study reached the same conclusion [23] when studying the effect of spatial resolution on precipitation forecasts over the central Andes of Peru, using GF in combination with YSU. They found an improvement in simulating accumulated precipitation by increasing the model's resolution from 18 to 3 km.

Using the New Tiedtke (NT) scheme, the spatial distribution of precipitation was better simulated than with the BMJ and KF parameterizations [24] over the Pacific Ocean and the Caribbean Sea. The same authors added that the BMJ and KF schemes, while worse, simulated the distribution of precipitation reasonably well, except for a general overestimation by the BMJ scheme and an underestimation in certain locations alongside overestimation in others using KF.

The main objective of the present study was to analyze the sensitivity of the WRF model to the use of different combinations of cumulus and planetary boundary layer

parameterization schemes, to evaluate which combination produced results most like observations in the region of interest.

To achieve this, the model's predictive capability was assessed using the results of a set of experiments conducted with WRF for a torrential rain episode that occurred during the El Niño Costero of 2017. This event occurred on 13–15 March over the central zone of Peru, in the Cordillera Blanca. During this episode, SENAMHI issued warnings for rains with moderate or strong intensity in the northern and southern parts of Peru and the central mountain range between 12 March and 16 March, https://www.senamhi.gob.pe, accessed on 1 December 2024. This event was selected due to its unique characteristics and the limited research available on El Niño Costero compared to other phases of the ENSO.

2. Materials and Methods

2.1. Case Study

The study conducted in this work focuses on the El Niño Costero that occurred during the austral summer (December to March) between 2016 and 2017. In the central Pacific (Region Niño 3.4), in December 2016, the SST showed an anomaly of −0.6 °C, which according to the value of the Oceanic Niño Index (ONI) corresponds to the presence of the cold phase of ENSO, that is, La Niña (ONI < −0.5 °C). In January 2017, slight anomalies of westerly winds were detected along the equatorial line along with a slight rise in SST, but the heat content remained around normal until February. Between March and mid-April, there was a shift in SST values from negative to positive, although they remained in the neutral range, getting closer to the threshold of +0.5 °C, which, if exceeded for three months, according to the ONI, indicates entering a warm phase of the ENSO [25].

Meanwhile, in the eastern Pacific, corresponding to the Niño 1 + 2 region (a quadrant that covers the northern part of the Peruvian sea), the SST anomaly was approximately +0.4 °C as early as December 2016. By the second week of January 2017, the increase in SST was at +0.9 °C, and anomalies of westerly winds appeared in the Eastern Equatorial Pacific. By February, the magnitudes reached were already above +2 °C and even +3 °C, while along the coast, near the cities of Talara and Paita, they were around +5 °C and +6 °C, respectively. Additionally, it should be noted that the mixed layer decreased by 6 m and deepened slightly during the first three months of the year [4]. This prompted the formation of the second band of the ITCZ, located off the coast of Peru, which led to the presence of precipitation characterized as very intense [26].

These temperature anomalies persisted until early April, when a retreat of the warmer waters to the north was observed, resulting in a decrease in the SST anomalies to values of +1 °C [25].

From the analysis of the synoptic conditions, it can be concluded that during the episode, a high-pressure area was located in the Pacific Ocean off the coast of Chile. This anticyclone reached its maximum on the 14th and began to weaken on the 15th. At altitude, relatively high temperatures were diagnosed at 850 hPa, with values between 16 and 24 degrees Celsius in practically the entire northern part of South America, with a high percentage of humidity throughout the episode analyzed. Cloudiness in the region was dominant and, on a synoptic scale, rains of convective origin were diagnosed mainly over Andean and coastal areas of Peru and the interior of Brazil. During this episode, SENAMHI issued warnings for rains with moderate or strong intensity in the northern and southern parts of Peru and the central mountain range between 12 March and 16 March.

2.2. Grid Data and Meteorological Stations

As reference datasets, this study used two different main sources of data. On the one hand, CHIRPS (Climate Hazards Group InfraRed Precipitation with Station) was selected

as a source of precipitation reference datasets. CHIRPS is a freely available global data source with daily precipitation estimates [27]. It uses satellite information with a resolution of 0.05° and daily precipitation estimates, available from 1981 to the present, covering regions between 50° N and 50° S latitude.

On the other hand, weather station datasets were considered. SENAMHI is the National Service of Meteorology and Hydrology of Peru. It is the institution responsible for providing meteorological and hydrological services in the country, including forecasting the weather, monitoring meteorological and climatic phenomena, and managing hydrological data to support decision-making in various sectors. From this institution, 20 meteorological stations were selected (Table 1), which were obtained from the official website (https://www.senamhi.gob.pe/?&p=estaciones, accessed on 1 December 2024). These stations cover all different latitudes, longitudes, altitudes above sea level, and proximities to the coast, as well as all climatic conditions over our study area.

Table 1. SENAMHI meteorological stations used in this study. The name, location (latitude and longitude), and accumulated precipitation (expressed in mm) over the 3-day event are shown for each station.

Name	Latitude	Longitude	Precipitation (mm)
Cabana	8°23′26.07″ S	78°0′16.60″ W	45.7
Sihuas	8°33′60.00″ S	77°39′0.00″ W	26.6
Pomabamba	8°49′18.13″ S	77°27′26.40″ W	16
Yungay	9°8′30.79″ S	77°44′59.91″ W	60.3
Aija	9°46′53.92″ S	77°36′24.26″ W	53.6
Huarmey	10°4′5.23″ S	78°9′44.35″ W	0.4
Chiquian	10°8′51.47″ S	77°9′34.18″ W	40.2
Dos de mayo	9°43′1.56″ S	76°46′25.46″ W	17.9
Jacas Chico	9°53′5.05″ S	76°30′3.37″ W	25.5
Chaglla	9°51′3.00″ S	75°54′25.40″ W	44.6
La divisoria	9°12′3.27″ S	75°48′50.15″ W	64.2
Camay	10°54′46.58″ S	77°38′56.03″ W	0
Paccho	10°57′21.67″ S	76°56′5.02″ W	48.7
Alcantarilla	11°3′38.45″ S	77°33′38.00″ W	0
Cerro de Pasco	10°41′36.15″ S	76°15′51.10″ W	16.7
Yanahuanca	10°29′22.57″ S	76°30′46.48″ W	17.7
Aguaytia	9°2′32.11″ S	75°30′22.46″ W	42.5
Aucayacu	8°55′47.53″ S	76°6′42.15″ W	60.4
Tingo Maria	9°18′36.60″ S	76°0′1.80″ W	82.1
Oxapampa	10°33′51.28″ S	75°25′6.41″ W	40.6

2.3. The WRF Model Setups

In this study, WRF with the Advanced Research WRF (WRF-ARW) dynamic core was used in its version 4.3.3. The simulations were completed with the configuration summarized in Table 2. It was based on two one-way nested domains: the outer domain (d01) spanning from 6.27203° to 14.28003° latitude, and from 82.548° to 72.34597° longitude, with a spatial resolution of 9 km. This area includes much of Peru and a small part of northwestern Brazil, as well as the entire Peruvian coast and the deep waters of the Pacific Ocean, as is shown in Figure 1. On the other hand, the inner domain (d02) covers the area from 8.23003° to 11.39197° latitude and from 79.99797° to 75.308° longitude, with a horizontal resolution of 3 km and 42 vertical levels.

Table 2. Summary of the WRF model configuration.

	d01	d02
Spatial resolution	9 km	3 km
Grid points and vertical levels (X, Y, Z)	125, 100, 42	172, 118, 42
Time step	54 s	18 s
Initial and boundary conditions	ERA-5	External domain
Spin-up	24 h	24 h

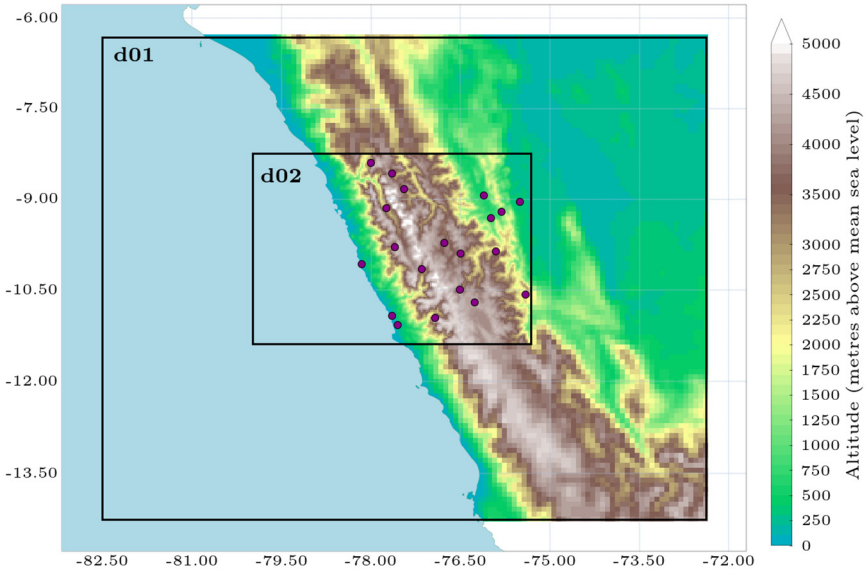

Figure 1. The WRF model domains: the outer domain (d01) with a 9 km spatial resolution and the inner domain (d02) with a 3 km spatial resolution. The locations of the 20 selected meteorological stations are shown as purple dots.

As initial and lateral boundary conditions (LBCs), the data provided by the fifth-generation reanalysis from the European Centre for Medium-Range Weather Forecasts (ERA5) [28] were used. ERA5 provides initial and boundary conditions at a resolution of 0.25°, which proved to be adequate for the study region [16,29,30]. The event was simulated from 12 to 15 March 2017, taking 12 March, i.e., the first 24 h, as the model's spin-up, and therefore not including it in the analysis. We used the 24 h spin-up time in our simulations to consider the importance of adequately stabilized atmospheric fields. Deeper research in this sense should be performed in the future. Usually, for short-term forecasts, 6 h [31,32] or 12 h [33] periods are typically used as spin-ups. But there are other studies that conclude that, depending on the meteorological situation, up to 36 h [34] or 48 h can be the optimum spin-up time [35,36]. In this sense, we selected 24 h as a balance between the widely used length and the longest period, which has also been used in other studies [36,37].

For the simulation time steps, the recommended values were used, i.e., 54 and 18 s for d01 and d02, respectively, corresponding to 6 times the spatial resolution of the corresponding domain [38].

A total of 22 experiments were conducted, which included combinations of two PBL schemes and six CU schemes, with the explicit resolution of the model being one of the six cumulus schemes mentioned (Table 3). Finally, the selected land surface model was Noah-MP [39], which is distinguished by its flexibility, accuracy, and ability to simulate complex processes at the land–atmosphere interface [40].

Table 3. Summary of the 22 experiments. Each column indicates the parameterization applied, with SWR and LWR representing the shortwave and longwave schemes, respectively; CU d01 and CU d02 are the convection schemes for the outer (d01) and inner (d02) domains, respectively; MPH refers to the microphysics scheme, PBL denotes the planetary boundary layer schemes, and LSM represents the land surface model. Radiation schemes, the land surface model, and microphysics schemes were fixed in this study.

Experiment	SWR	LWR	CU d01	CU d02	MPH	PBL	LSM
Y_BMJ	RRTMG	RRTMG	BMJ	BMJ	THO	YSU	Noah-MP
Y_GD	RRTMG	RRTMG	GD	GD	THO	YSU	Noah-MP
Y_GF	RRTMG	RRTMG	GF	GF	THO	YSU	Noah-MP
Y_KF	RRTMG	RRTMG	KF	KF	THO	YSU	Noah-MP
Y_NT	RRTMG	RRTMG	NT	NT	THO	YSU	Noah-MP
Y_BMJ_OFF	RRTMG	RRTMG	BMJ	Deactivated	THO	YSU	Noah-MP
Y_GD_OFF	RRTMG	RRTMG	GD	Deactivated	THO	YSU	Noah-MP
Y_GF_OFF	RRTMG	RRTMG	GF	Deactivated	THO	YSU	Noah-MP
Y_KF_OFF	RRTMG	RRTMG	KF	Deactivated	THO	YSU	Noah-MP
Y_NT_OFF	RRTMG	RRTMG	NT	Deactivated	THO	YSU	Noah-MP
M_BMJ	RRTMG	RRTMG	BMJ	BMJ	THO	MYJ	Noah-MP
M_GD	RRTMG	RRTMG	GD	GD	THO	MYJ	Noah-MP
M_GF	RRTMG	RRTMG	GF	GF	THO	MYJ	Noah-MP
M_KF	RRTMG	RRTMG	KF	KF	THO	MYJ	Noah-MP
M_NT	RRTMG	RRTMG	NT	NT	THO	MYJ	Noah-MP
M_BMJ_OFF	RRTMG	RRTMG	BMJ	Deactivated	THO	MYJ	Noah-MP
M_GD_OFF	RRTMG	RRTMG	GD	Deactivated	THO	MYJ	Noah-MP
M_GF_OFF	RRTMG	RRTMG	GF	Deactivated	THO	MYJ	Noah-MP
M_KF_OFF	RRTMG	RRTMG	KF	Deactivated	THO	MYJ	Noah-MP
M_NT_OFF	RRTMG	RRTMG	NT	Deactivated	THO	MYJ	Noah-MP
M_OFF	RRTMG	RRTMG	Deactivated	Deactivated	THO	MYJ	Noah-MP
Y_OFF	RRTMG	RRTMG	Deactivated	Deactivated	THO	YSU	Noah-MP

2.4. Evaluation Methods

The evaluation was based on comparing precipitation outputs with observational values. First, a spatial comparison of the accumulated precipitation throughout the entire event was carried out, representing the precipitation for each of the experiments in both domains (d01 and d02) and for CHIRPS, with the objective of comparing the spatial patterns of precipitation during the event. In this case, both the simulations and the reference values were used in their native resolution, to produce results without adding uncertainties due to interpolation techniques.

In a second analysis, focusing solely on the results from d02, which is the domain of interest, the relative bias expressed as a percentage was calculated according to Equation (1).

$$\text{Bias}(\%) = \frac{1}{N}\sum_{i=1}^{N}\frac{P_i - O_i}{O_i} \quad (1)$$

where P_i represents the simulated accumulated precipitation at each moment, *Oi* the precipitation estimated by CHIRPS, and N the number of observations. This analysis allows for evaluating how well the model reproduces the precipitation event, identifying both overestimations and underestimations compared to CHIRPS data. Since the grid used by CHIRPS is different from that of WRF outputs, all WRF data were interpolated to the CHIRPS grid using nearest neighbor interpolation via Climate Data Operators (CDOs) [41].

Then, a comparison with stations was conducted to quantify the model's deviations concerning actual point values of daily precipitation. This analysis was also performed using CHIRPS to highlight differences between precipitation data from stations and CHIRPS estimates. For the comparison of model outputs and CHIRPS with stations, the average precipitation from the four nearest neighbors to the study station was considered.

To verify the precipitation prediction capability of the model, different statistical indices comparing simulated and observed precipitation values were calculated. On the one hand, a deterministic numerical validation was carried out, based on the calculation of indices such as the relative bias error (Equation (1)), the Pearson correlation coefficient (R, Equation (2)), and the relative root mean square error (RRMSE, Equation (3)).

$$R = \frac{N\left[\sum_{i=1}^{N}(P_i\,O_i)\right] - (\sum_{i=1}^{N}P_i)(\sum_{i=1}^{N}O_i)}{\left[N\sum_{i=1}^{N}(P_i)^2 - (\sum_{i=1}^{N}P_i)^2\right]^{1/2}\left[N\sum_{i=1}^{N}(O_i)^2 - (\sum_{i=1}^{N}O_i)^2\right]^{1/2}} \quad (2)$$

$$\text{RRMSE}\ (\%) = \left(\frac{\left[N^{-1}\sum_{i=1}^{N}(P_i - O_i)^2\right]^{1/2}}{\overline{O}}\right) \times 100 \quad (3)$$

where $\overline{O}$ is the average value of O_i. Note that in this case, we considered the records from 3 days and 20 stations, so N was 60 (3 days multiplied by 20 stations).

On the other hand, categorical validation was employed [42]. For this method, the forecast of a categorical event can be represented as the occurrence or non-occurrence of the event, as well as the surpassing of a significant threshold [20]. This form of verification is performed using a contingency table (Table 4), where A, B, C, and D represent the number of occurrences of each individual verification.

Table 4. Contingency table for precipitation verification.

Observation			
Yes	**No**		
A	B	Yes	Forecast
C	D	No	

From Table 4, the Probability of Detection (POD), False Alarm Ratio (FAR), Frequency Bias (FBI), and Critical Success Index (CSI) are obtained.

The POD (Equation (4)) is the ratio of hits (when an event is forecasted and occurs) to the total number of forecasted events. This metric measures the model's ability to predict the occurrences of the event in question. A value of 1 means that the model has correctly identified all events that occurred, while a lower value indicates a reduced accuracy in detecting the events.

$$\text{POD} = \frac{A}{A + C} \quad (4)$$

The FAR (Equation (5)) is the proportion of false alarms relative to the total number of predictions made by the model. In other words, it measures the rate of locations or moments in which the model incorrectly predicted the occurrence of an event that did not actually occur. A FAR of 0 indicates a perfect forecast, where no false alarms were made, while a higher value indicates a greater frequency of false alarms in the model's predictions.

$$\text{FAR} = \frac{B}{B + C} \quad (5)$$

The FBI (Equation (6)), on the other hand, shows the model's tendency to overestimate or underestimate the occurrence of an event. When the FBI is greater than 1, it indicates that the model tends to overestimate the number of events. If the FBI is less than 1, the model tends to underestimate the occurrence of the event, and if it equals 1, the model's

prediction is perfect regarding the event's frequency, although not necessarily in terms of exact location or timing.

$$\text{FBI} = \frac{A+B}{A+C} \tag{6}$$

Finally, the CSI (Equation (7)) indicates how well the exceedances of a threshold are predicted, considering false alarms and unpredicted exceedances. A CSI of 1 would indicate a perfect prediction, while a CSI of 0 would indicate the opposite.

$$\text{CSI} = \frac{1}{\frac{1}{(1-FAR)} + \frac{1}{POD} - 1} = \frac{A}{A+B+C} \tag{7}$$

It is important to note that a POD forecast equal to 1 does not indicate that the predictions are highly reliable, just as a FAR of 0 does not imply reliability. In any case, to achieve a proper view of the accuracy of the simulations, an analysis of the four statistics (POD, FAR, FBI, and CSI) was performed.

For this type of analysis, two thresholds were set: a threshold of 1 mm to define whether the model can detect the occurrence of a rainy day, and another of 10 mm, which translates to heavy precipitation during a day at each meteorological station. These contingency tables were constructed for all simulations performed, and the various metrics were calculated.

3. Results

3.1. Spatial Patterns of the Study Event

Figure 2 shows the 3-day accumulated precipitation from simulations conducted with the YSU PBL for both domains (d01 and d02). The left column represents the results for the outer domain (d01), zoomed in to the size of the inner domain for easier comparison. The center column shows the results when the same cumulus parameterization is used in both domains, and the right column presents the simulations using the same cumulus parameterization for d01, but with CU switched off for d02. Additionally, CHIRPS-estimated precipitation has been added in the first row.

Compared to CHIRPS (Figure 2), it can be seen that the model tends to overestimate precipitation in mountainous regions (values up to 250 mm or more) where CHIRPS shows a maximum precipitation of up to 50 mm. While CHIRPS locates a maximum in the northwest of the domain, where up to 150 mm is reached, only the Y_GF and Y_KF experiments seem to adequately capture this precipitation. In contrast, Y_BMJ and Y_NT appear to have the most difficulty characterizing this maximum in both domains. It is worth noting that the simulations agree with CHIRPS in the absence of rain along the coast.

Concerning differences between the two domains, the results clearly show the effect of an increasing resolution, as the precipitation patterns in d02 (center and right columns) are finer and more detailed, capturing greater variability in precipitation intensities and spatial distribution. In this domain, there is also an intensification of precipitation in certain areas that is not clearly detected in domain d01 (left column). The results in d02 seem to be more aligned with the CHIRPS pattern in terms of precipitation distribution and levels compared to those in d01, suggesting that the increase in spatial resolution provides better results capturing the total precipitation of this event.

Regarding the differences between using convection on and off in d01 (center and right columns in Figure 2), we see that deactivation seems to result in more dispersed precipitation towards the northeast of the domain, leading to an absence of precipitation at the domain's borders that is more pronounced in Y_BMJ and Y_NT. The Y_KF_OFF and Y_GF_OFF experiments appear to better capture the precipitation distribution for this event compared to CHIRPS.

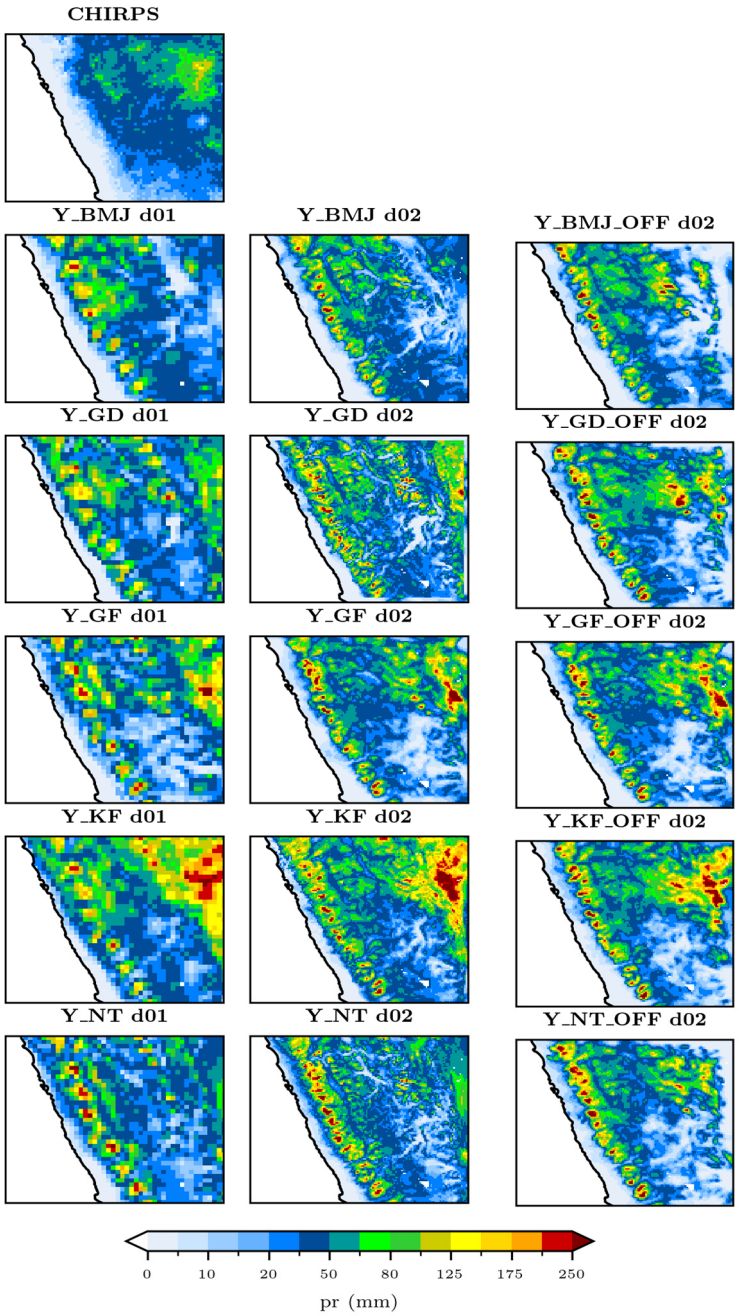

Figure 2. Accumulated precipitation of the event for simulations under the YSU PBL. The first row shows the accumulated precipitation in CHIRPS (reference data), and from the second row onward, each row corresponds to a cumulus parameterization. The left column shows the results for d01. The center column shows parameterization in both domains. The right column shows parameterization in d01 and the explicit resolution in d02.

Figure 3 shows the same analysis, but using MYJ as the PBL. Under this PBL, the model resolution (right column) localizes the rain more accurately, with higher intensities in certain areas or, conversely, as can be seen in M_KF_OFF d02, almost no rain at all.

When parameterization is resolved in both domains (center column), the results show that the model tends to generate an amount of precipitation more similar to CHIRPS than those with CU deactivated in d02. In this region, the experiments M_GD and M_KF appear to produce better predictions compared to CHIRPS in d02. However, part of the overestimation shown over mountain ranges in d01 is corrected for d02. Simulations with cumulus parameterization, moreover, especially those combined with KF, GD, and NT CU

parameterizations, produce significant precipitation in the northeastern region, covering a large area expected to be affected by rain, similar to the CHIRPS forecast.

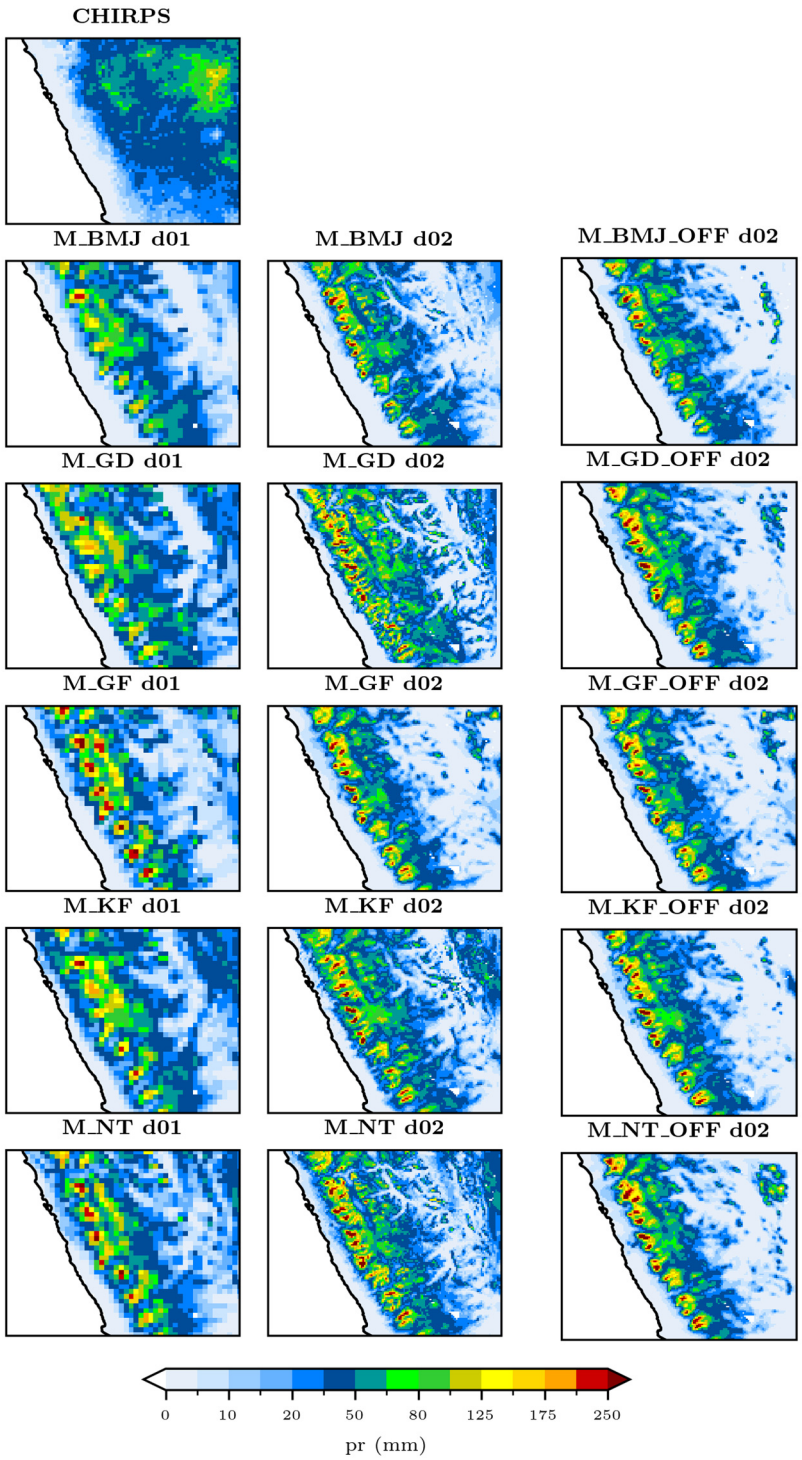

Figure 3. As Figure 2, but for MYJ PBL.

Regarding the differences between experiments in the inner domain (central column), M_BMJ and M_GF seem to show less precipitation in the east compared to other experiments. M_GD, however, displays precipitation over a larger portion of the domain, with maximum intensities as strong as those observed in other simulations (i.e., M_KF and M_NT), which also show areas of intense precipitation concentrated along the mountain range.

When the cumulus parameterization is deactivated in d02 (right column), we observe, as in the case of YSU, a reduction in precipitation in the western region of the domain. In this case, such deactivation seems to lead to a general worsening of the results. Thus, in the northeastern region, only M_NT_OFF is able to forecast precipitation in a small area, considering the large amount of precipitation predicted by CHIRPS.

Figure 4 shows the results of those experiments in which convection was deactivated in both domains. If we compare Y_OFF d02 and M_OFF d02, we can see that the simulation with PBL YSU is more similar to CHIRPS than that with MYJ. That is, MYJ produces more precipitation in the high mountain areas, but in the places where CHIRPS forecasts higher accumulations, this simulation hardly forecasts any rainfall. Y_OFF d02 captures the northeastern precipitation shown in CHIRPS (albeit with higher intensities), and it also predicts more intense rainfall north of the Cordillera Blanca than in the south, making it a very good simulation.

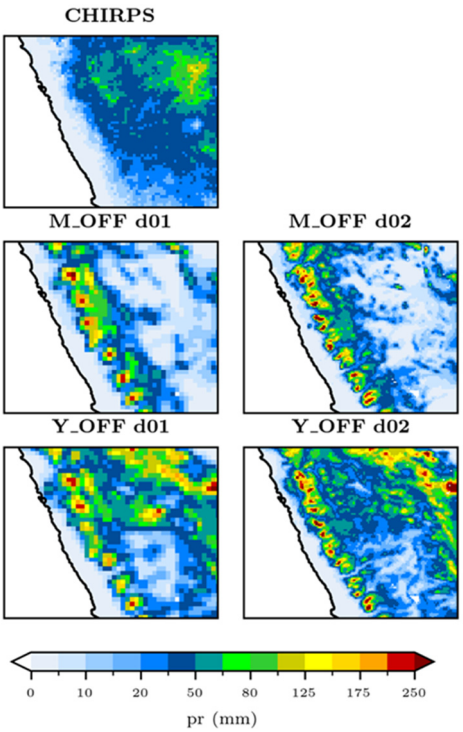

Figure 4. The 3-day accumulated precipitation for simulations with an explicitly resolved CU in both domains and for the two PBLs evaluated.

Figure 5 shows the relative bias for d02 expressed in percentage terms for experiments completed with YSU PBL. In the first column, the results for the different combinations with the convection switched off in d02 are shown, with the CU indicated for d01. In the second colum, the same experiments but with the CU activated are shown. The BMJ parameterization experiments (first row) show an underestimation of precipitation in the northwest in both simulations, though it seems more pronounced in Y_BMJ_OFF, with relative bias values reaching as low as −70%. Meanwhile, in the southwest region, Y_BMJ tends to overestimate precipitation more compared to Y_BMJ_OFF, which exhibits a more moderate bias. Y_GD shows a more uniform bias when compared to Y_GD_OFF in the central part of the map. However, in the northern part, both experiments tend to underestimate the precipitation, though Y_GD_OFF shows a more marked bias. As for the experiments applying the GF scheme, the results show very similar bias patterns in the eastern zone. This is also true towards the coast, where Y_GF_OFF seems to slightly underestimate more than its counterpart, but the results are very similar. Among the

KF experiments, the cumulus-parameterized resolution underestimates less in the central and southern parts of the domain. However, Y_KF_OFF is more balanced in the eastern zone, though both simulations tend to overestimate precipitation. Lastly, NT convection experiments show a more moderate bias in the central area, while the Y_NT_OFF version displays a more intense bias, both in underestimation and overestimation. Moreover, in the southern zone, Y_NT_OFF generates greater underestimation than Y_NT, while it overestimates more in the mountainous region.

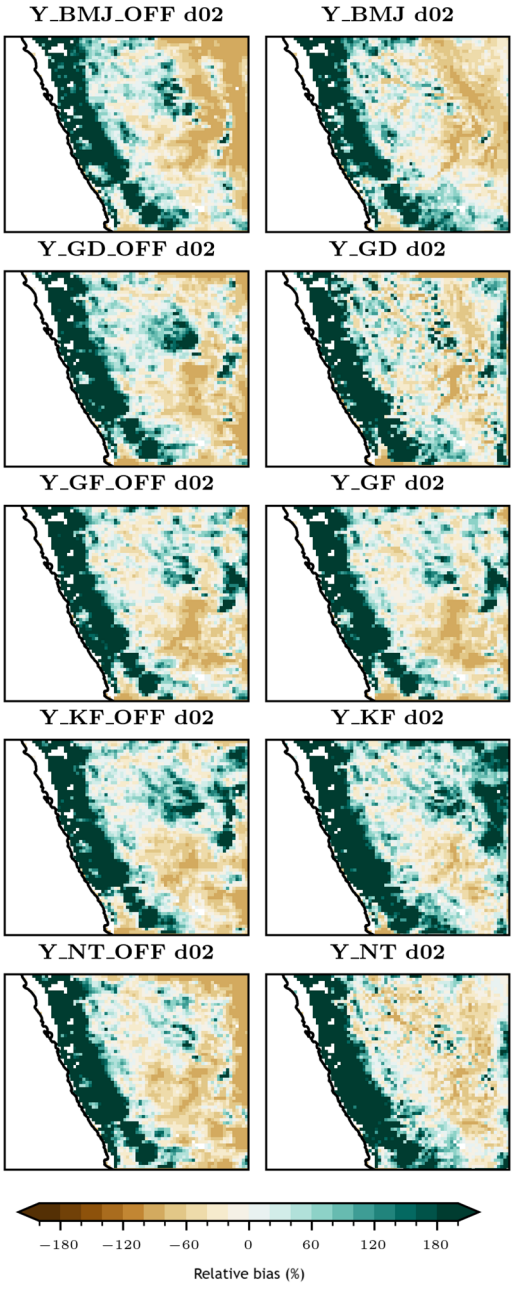

Figure 5. Relative bias (%) of experiments completed with YSU PBL when compared to CHIRPS.

Although no forecast is perfect, the simulations with cumulus parameterization in d02 (right column) appear to better capture the spatial variability of precipitation compared to the explicit-resolution versions. Of all of them, Y_NT seems to outperform the remainder, showing a smaller relative bias in several key regions.

Figure 6 shows the relative bias results for experiments completed with MYJ PBL. When comparing the experiments where convection is deactivated in d02 (i.e., with names

ending in _OFF) with those where it remains active, M_BMJ_OFF (first row) shows a more extensive and pronounced underestimation (up to −100%) compared to M_BMJ in the east and northeast of the region. In the south, both simulations overestimate precipitation, but M_BMJ has a more localized and intense overestimation. In the case of GD experiments, M_GD_OFF underestimates much of the central area, but less intensely than M_GD, which shows a clearer underestimation pattern in the center and east. M_GF_OFF and M_GF show a very similar overestimation in the northern part. However, for the central and southern zones, the first shows a more dispersed negative bias, while M_GF has a more concentrated underestimation in certain areas. Again, these differences are small, so it can be said that both results are similar. Overall, M_KF shows a more pronounced overestimation specifically over the Andes, while M_KF_OFF presents greater underestimations over the northeastern part of the domain d02 where the topography is lower. When comparing the two NT experiments, the explicit-resolution simulation significantly underestimates in the central–southern and eastern areas. However, both simulations exhibit a similar overall underestimation pattern.

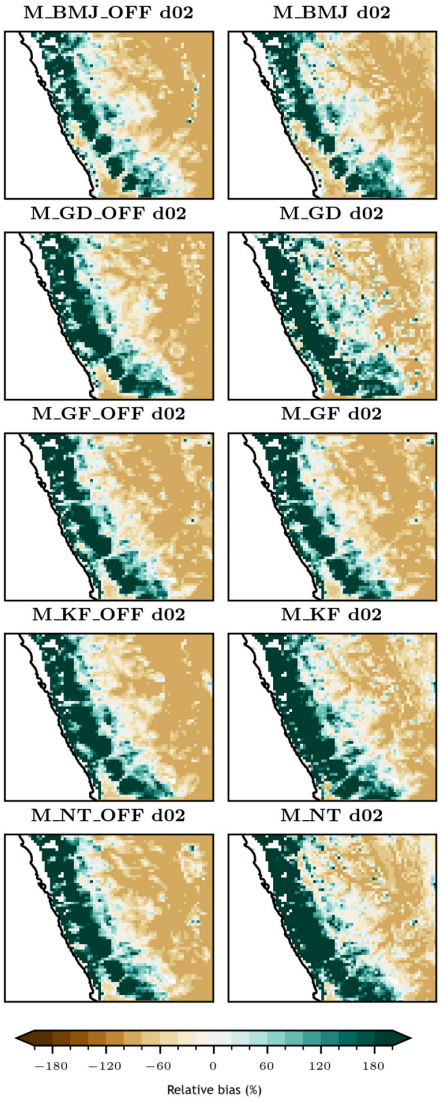

Figure 6. Comparison of the relative bias (%) of the experiments for the d02 domain with respect to CHIRPS using the MYJ PBL.

Finally, Figure 7 shows the simulations with convection deactivated in both domains, using the MYJ PBL (M_OFF d02) and YSU PBL (Y_OFF d02). In general, the model exhibits

a high sensitivity to the PBL scheme. Y_OFF appears to be more suitable, as it generates less underestimation of precipitation in the northern, central, and southern parts of the domain compared to M_OFF. If we compare the Y_OFF experiment with the rest of the YSU PBL simulations, it shows a significant reduction in the overestimation of precipitation in the eastern parts of the domain, though it remains imperfect, with underestimation areas like those in the other experiments. Meanwhile, M_OFF generates patterns much more similar overall to the rest of the MYJ experiments.

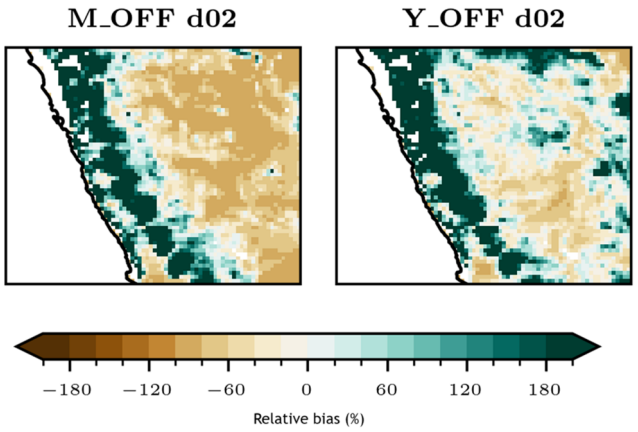

Figure 7. Relative bias (%) for both PBLs with the explicit resolution of the model in both domains.

After analyzing the three relative bias figures and considering the distribution of the values obtained, the best simulation appears to be Y_OFF d02. This simulation, which uses YSU as the PBL and has cumulus parameterization deactivated for both domains, reduces precipitation underestimations more effectively than the rest. It also performs more balanced and consistently in most regions, demonstrating an improved capacity to handle regional variability compared to the other simulations. For this reason, Y_OFF d02 is the most robust and accurate simulation for the conditions evaluated.

3.2. Deterministic Numerical Validation

The results of deterministic numerical validation (Relative Bias, R, RRMSE) and categorical validation (POD, FAR, FBI, and CSI) are presented below. Additionally, CHIRPS was also validated to determine the similarity between the two reference datasets. The analysis was performed only for the inner domain (d02), just as it was with the relative biases, since this is the final domain of interest.

Table 5 shows the deterministic numerical evaluation for all experiments and CHIRPS. For the latter, the results show a bias of −23%, a correlation of 0.41, and an RRMSE of 94.99%, indicating that CHIRPS, compared to stations, captured less precipitation for this event. This evidences the importance of using different reference datasets when evaluating results.

Compared to stations, the WRF experiments show relative biases ranging from −20.15% (Y_KF) to −80.95% (M_OFF), indicating that, in general, WRF underestimates the precipitation in this region. The results also show that YSU PBL tends to produce a lower relative bias compared to simulations using MYJ, indicating the better agreement of YSU with stations. Regarding the effect of activating or deactivating convection in the inner domain (i.e., d02 OFF or ON), simulations with activated convection generally produce a lower bias than those where convection is disabled, although this effect is not very pronounced. This is replicated when we deactivate the parameterization in both domains for MYJ (M_OFF). In contrast, Y_OFF yields a better value than other experiments with YSU. When comparing the different cumulus parameterizations, BMJ, when combined

with YSU, shows a tendency to significantly underestimate precipitation, generating one of the highest biases compared to other convection schemes. However, NT and GD, when used with YSU, tend to show a less pronounced bias, making them more suitable for this region. The value closest to the ideal is found in Y_KF (−20.15%), being the best among the experiments, thus achieving a more accurate representation of precipitation, making it the most effective scheme for this region in our case study in terms of relative bias.

Table 5. Results of the deterministic numerical validation for CHIRPS and the WRF experiments. CHIRPS values are shown in the first row, and the three experiments with the worst and the best values for relative bias, R, and RRMSE are shown in bold.

Experiment	Relative Bias (%)	R	RRMSE (%)
CHIRPS	−23	0.41	94.99
Y_BMJ	−65.3	−0.04	126.9
Y_GD	−49.32	**0.33**	**108.08**
Y_GF	−57.77	0.12	120.24
Y_KF	**−20.15**	**0.27**	121.17
Y_NT	−37.63	**0.27**	**107.78**
Y_BMJ_OFF	−60.85	−0.06	130.1
Y_GD_OFF	**−35.42**	0.16	123.75
Y_GF_OFF	−48.71	0.19	116.78
Y_KF_OFF	**−29.49**	0.22	120.78
Y_NT_OFF	−49.2	0.23	118.7
Y_OFF	−42.93	0.34	**108.34**
M_BMJ	−73.61	**−0.13**	133.05
M_GD	−68.19	**−0.16**	133.37
M_GF	**−79.89**	−0.11	135.04
M_KF	−59.19	−0.07	130.45
M_NT	−64.6	−0.11	133.45
M_BMJ_OFF	−71.73	−0.11	**135.20**
M_GD_OFF	−75.77	−0.09	134.35
M_GF_OFF	−78.42	**−0.12**	134.52
M_KF_OFF	−73.92	−0.09	133.77
M_NT_OFF	**−79.24**	**−0.12**	**136.02**
M_OFF	**−80.95**	−0.11	**136.04**

In terms of correlation, simulations with YSU seem to capture better this event, with positive correlations greater than 0.20 in many cases. However, experiments with MYJ yield negative correlation values. In terms of using the parameterization scheme in d02, the results suggest that using convection parameterizations is more appropriate for characterizing precipitation at 3 km. However, when deactivating the parameterization in both domains (Y_OFF), the highest value of R (0.34) is obtained, positioning it as the best among the experiments. Similar conclusions are obtained to those reached with the relative bias in terms of R when the boundary layer is compared.

Finally, the RRMSE values for the different experiments compared cover a range from 107.78% (Y_NT) to 136.04% (M_OFF), with the results from experiments with YSU overall outperforming the others. On the other hand, RRMSE seems to indicate that, at least in this region and for this specific event, the experiments with parameterization in the inner domain yield the best results. Moreover, RRMSE indicates that BMJ is not a good scheme for this region as it tends to generate one of the greatest errors. In contrast, the GD and NT schemes stand out among the rest for having the lowest biases.

3.3. Categorical Validation

For categorical validation (POD, FAR, FBI, and CSI), Tables 6 and 7 present the results for thresholds of 1 mm and 10 mm, respectively.

Table 6. Results of the categorical validation when a 1 mm threshold is used. In the first row are the values of CHIRPS; in bold are the three experiments with the worst and the best values for POD, FAR, FBI, and CSI.

Experiment	POD	FAR	FBI	CSI
CHIRPS	1	0.04	1.04	0.96
Y_BMJ	0.9	**0.02**	0.92	0.88
Y_GD	**1**	0.04	**1.04**	**0.96**
Y_GF	0.84	**0.02**	0.86	0.82
Y_KF	**0.94**	0.04	**0.98**	**0.9**
Y_NT	**1**	0.04	**1.04**	**0.96**
Y_BMJ_OFF	0.65	0.03	0.67	0.64
Y_GD_OFF	0.65	0.03	0.67	0.64
Y_GF_OFF	0.78	0.03	0.8	0.76
Y_KF_OFF	0.78	0.03	0.8	0.76
Y_NT_OFF	0.65	0.03	0.67	0.64
Y_OFF	0.84	**0.02**	0.86	0.82
M_BMJ	0.69	**0.56**	0.73	0.67
M_GD	0.69	**0.06**	0.73	0.67
M_GF	**0.41**	0.05	**0.43**	**0.4**
M_KF	0.76	0.05	0.8	0.73
M_NT	0.88	0.04	0.92	0.84
M_BMJ_OFF	**0.35**	**0.06**	**0.37**	**0.34**
M_GD_OFF	**0.41**	0.05	**0.43**	**0.4**
M_GF_OFF	**0.41**	0.05	**0.43**	**0.4**
M_KF_OFF	**0.41**	0.05	**0.43**	**0.4**
M_NT_OFF	**0.41**	0.05	**0.43**	**0.4**
M_OFF	**0.35**	**0.56**	**0.37**	**0.34**

Table 7. As Table 6 but for a 10 mm threshold.

Experiment	POD	FAR	FBI	CSI
CHIRPS	0.57	0.41	0.96	0.41
Y_BMJ	0.21	0.5	0.43	0.18
Y_GD	0.29	0.47	0.54	0.23
Y_GF	0.25	0.53	0.54	0.19
Y_KF	0.36	**0.44**	0.64	0.28
Y_NT	**0.46**	**0.46**	**0.86**	**0.33**
Y_BMJ_OFF	0.32	0.5	0.64	0.24
Y_GD_OFF	**0.43**	0.5	**0.86**	**0.3**
Y_GF_OFF	0.29	**0.56**	0.64	0.21
Y_KF_OFF	**0.61**	**0.43**	**1.07**	**0.41**
Y_NT_OFF	0.32	0.5	0.64	0.24
Y_OFF	0.29	**0.56**	0.64	0.21
M_BMJ	0.14	**0.56**	**0.32**	**0.12**
M_GD	0.18	**0.58**	**0.43**	0.14
M_GF	**0.07**	**0.67**	**0.21**	**0.06**
M_KF	0.18	**0.58**	**0.43**	0.14
M_NT	**0.11**	**0.67**	**0.32**	**0.09**
M_BMJ_OFF	0.29	0.47	0.54	0.23
M_GD_OFF	0.14	**0.56**	**0.32**	**0.12**
M_GF_OFF	**0.11**	**0.67**	**0.32**	**0.09**
M_KF_OFF	**0.11**	**0.67**	**0.32**	**0.09**
M_NT_OFF	**0.07**	**0.67**	**0.21**	**0.06**
M_OFF	**0.11**	**0.67**	**0.32**	**0.09**

For a 1 mm threshold (Table 6), CHIRPS shows a POD of 1, a FAR of 0.04, an FBI of 1.04, and a CSI of 0.96. These values indicate that CHIRPS has an adequate detection capability for the event in question when compared to stations.

In general, experiments with YSU show better results than those with MYJ, reaching values of up to 1 in the case of Y_GD and Y_NT. On the other hand, for the MYJ PBL, the

best result is for M_NT (POD of 0.88). This suggests that the YSU PBL is more suitable than MYJ for detecting precipitation, at least for this event. When comparing experiments with active parameterization against those with explicitly resolved convection in d02, it is observed that the POD values are higher when the parameterization is active. For example, Y_GD and Y_NT have POD values of 1, while their OFF versions have a POD of 0.65. These results suggest that activating convection in d02 provides better results in detecting precipitation occurrence. However, if the parameterization is deactivated in both domains (Y_OFF), the value is very similar to those obtained for the active parameterizations in d02.

The FAR measures the proportion of events that a model predicts but that do not materialize, that is, the fraction of prediction errors in relation to all predicted values. The results show that FAR values for experiments using YSU are generally lower. For example, Y_BMJ and Y_GF present a FAR of 0.02. This contrasts with experiments using MYJ, which show higher values, reaching a maximum when the BMJ convection is activated for both domains, where FAR reaches 0.56. When comparing models with active parameterization against those with explicitly resolved convection in d02, it can be observed that the values are quite similar, except for the case of BMJ experiments, where a much higher value is reached when convection is activated (FAR of 0.56 vs. 0.06).

The FBI provides a measure of the model's tendency to overestimate (FBI > 1) or underestimate (FBI < 1) events. Values equal to 1 indicate a perfect prediction. In the comparison of experiments with different PBLs, the results again suggest that YSU is better at detecting the precipitation event analyzed here (values between 0.67 and 1.04). Experiments with MYJ, however, show values of 0.37 and 0.8, suggesting that MYJ generally tends to underestimate. When comparing experiments with active cumulus parameterization against those with resolved convection, models with active parameterization tend to generate values closer to 1, indicating better correspondence between the forecast and observation. In terms of convection parameterization, KF seems to be the best; in combination with YSU, it results in an almost perfect FBI (FBI of 0.98). Concerning the results in terms of CSI (values between 0 and 1, with 1 being a perfect fit), similar conclusions can be drawn as with the other metrics, as experiments with YSU and parameterized convection in d02 generate better results, with KF being a generally suitable parameterization. As for the best combinations, Y_GD and Y_NT present the best CSI values (0.96), reflecting an excellent detection capability that equals that of CHIRPS.

For the 10 mm precipitation threshold (Table 7), the results show a general decrease in skill for both CHIRPS and the different WRF experiments. This was expected given the stricter threshold. Thus, CHIRPS has a POD value of 0.57, a FAR of 0.41, an FBI of 0.96, and a CSI of 0.41. As for the 1 mm threshold, simulations performed with YSU seem to be more suitable for detecting intense precipitation (above 10 mm), as they generally present higher POD values (up to 0.61 for Y_KF_OFF vs. 0.29 for Y_BMJ_OFF), lower FAR values (around 0.5 for YSU vs. 0.6 for MYJ), and FBI values closer to 1, although they tend to underestimate the detection of intense precipitation, also showing higher CSI values. However, the results between activating or deactivating the convection parameterization for d02 are not so clear and sometimes depend on the PBL used. For YSU, if the model resolves convection explicitly, the POD values are higher, and therefore better than with active parameterization, except for Y_NT. Conversely, for MYJ, POD is better for most experiments with active cumulus parameterization. This also holds when deactivating the parameterization in both domains for the two PBLs (Y_OFF and M_OFF). Finally, the experiment Y_KF_OFF stands out for having the highest POD (0.61), even surpassing that of CHIRPS. In terms of FAR, activation or deactivation leads to similar values, with better FBI values when convection is deactivated, at least when using YSU. Regarding CSI, the values are very similar. If there is one cumulus parameterization to highlight over the rest, it would be KF, which presents

some of the best results in all its combinations, especially Y_KF_OFF with an FBI value of 1.07, indicating good performance of the experiment despite occasional overestimation. In fact, for a 10 mm threshold, it can be concluded that the Y_KF_OFF experiment stands out compared to the rest, being the best in terms of POD (0.61), FAR (0.43), FBI (1.07), and CSI (0.41). Therefore, this experiment can be considered the best in terms of overall results, even surpassing CHIRPS in some metrics.

4. Discussion

The results obtained in this study provide a detailed insight into the sensitivity of the WRF model when simulating precipitation during El Niño Costero events in the Andean region of Peru. In this context, the results obtained for YSU are better than those for MYJ when compared to CHIRPS in terms of spatial results. This is consistent with the conclusions of Rojas and Rojas [43], who found that YSU is more suitable for simulating precipitation events in Peru. This is because YSU performs better in the study area due to its superior ability to model mixing and convection processes in the atmospheric boundary layer compared to other PBLs [44].

As shown in the results, the influence of spatial resolution and cloud parameterization on precipitation simulation is another crucial aspect. In this regard, a study by Moya-Álvarez et al. [23] highlighted that increasing the spatial resolution improves the simulation of accumulated precipitation. However, as these authors argue, the model still faces challenges with local storms. In this work, through the subjective comparison of spatial patterns between domains, it was found that increasing the resolution in d02 allows for a more detailed representation of spatial variability and precipitation intensity.

Regarding cloud parameterizations, those using BMJ in any of the domains stand out for their poor performance in this case study. These results agree with several studies (e.g., [24,45]) that advise against using this convection scheme. The best cloud parameterization was proven to be KF for both PBLs due to its similarity to CHIRPS (Figures 2 and 3), especially when combined with YSU, which is consistent with another study [16]. Additionally, Y_KF_OFF also provides good results compared to the experiment with parameterization in both domains. This result occurs because at low resolutions, the model operates almost explicitly. The latter agrees with the results found in Solano-Farias et al. [46], who analyzed the WRF sensitivity for long-term simulations over the south of Spain. Despite this, overestimations over regions with complex topography were high in all experiments, a similar result to other studies such as that by Mourre et al. [22], who emphasized the need to fine-tune the resolution and parameterizations to improve simulations in high mountain areas.

Regarding the relative biases (Figures 5 and 6), the NT and KF scheme is positioned as the best of the five evaluated, thanks to presenting a greater balance between overestimation in high mountain regions and underestimation in the northeastern part of the domain. The good performance of this scheme is due to its consideration of deep, medium, and shallow convection [24]. However, it has been observed that an explicit resolution for both domains, when combined with YSU, provides good results. That is, these are the experiments with the best results in terms of relative bias, as also indicated by Han and Hong [47] using domains similar to those in our study.

It is important to highlight that the dependence on CHIRPS as a reference introduces a level of uncertainty, given that this database also has its limitations in estimating precipitation, especially presenting relatively low accuracy on a daily scale [48]. On the other hand, the 20 selected meteorological stations are not free from errors, especially considering some locations in high mountain areas [49].

From the results of the deterministic numerical and categorical evaluations, a general trend of the model to underestimate precipitation is observed, particularly in configurations that use MYJ as the PBL scheme and in those where convection is resolved explicitly by the model. This negative bias, particularly pronounced in the M_OFF configuration, suggests that these configurations are less suitable for the study area. In contrast, simulations employing YSU show a reduction in relative bias compared to those using MYJ. This finding coincides with the results of previous analyses. However, it is important to recognize that, despite being less pronounced, underestimation remains significant.

Regarding cloud parameterizations, the results of this analysis confirm BMJ was the worst of the five evaluated, as could be seen in the figures of the spatial results. Experiments using KF and NT appear to be more suitable. It should be noted that KF in d01 and the explicit resolution in d02 (i.e., Y_KF_OFF) perform better for stronger precipitation, as can be seen with the categorical validation at a 10 mm threshold. In contrast, if the aim is to capture the presence of rain (1 mm/day threshold), the Y_NT experiment is ideal due to its CSI values.

On the other hand, and as mentioned in the results of the spatial analyses, the Y_OFF experiment offers a good forecast for detecting the presence of precipitation (1 mm/day threshold), while for intense precipitation events (10 mm/day threshold), this experiment tends to underestimate precipitation. This confirms the findings of Han and Hong [47], who found that disabling parameterization schemes resulted in a better performance for light precipitation in nested domains of 3, 9, and 27 km.

Despite all these findings, it is crucial to emphasize the need to explore additional configurations or improve existing parameterizations to better address the important role of orography as a triggering mechanism for convection in cloud schemes [50]. Furthermore, to improve precipitation prediction capabilities in the simulations of this study, it would be interesting to assess the effectiveness of a wider variety of parameterizations, PBLs, and domain configurations for this and other extreme precipitation events over Peru, as well as to implement different microphysics schemes, which have been shown to play a significant role in precipitation development [51].

5. Conclusions

In the present study, a sensitivity study of WRF physics schemes was evaluated. This focused on a torrential precipitation event that occurred from 13 March to 15 2017, under El Niño Costero conditions in areas of Peru. For this purpose, different combinations of parameterizations were used in a total of 22 experiments, including the combination of two boundary layer schemes (YSU and MYJ), five different cloud parameterizations (BMJ, KF, GF, GD, and NT), as well as the explicit resolution of convection by the model itself.

From the obtained results, the following conclusions can be drawn regarding the behavior of the WRF model in simulating this event for our study area:

- The WRF model exhibits significant sensitivity to the selection of the boundary layer scheme: YSU can detect the simulated event better than MYJ. Simulations that use YSU result in lower errors, better correlation, and a greater ability to capture the spatial variability of precipitation.
- The model is sensitive to an increased spatial resolution: When comparing the simulations obtained, it can be seen that increasing the domain from 9 km to 3 km allows for better capture of precipitation patterns, especially in areas with complex topographies.
- Activating or deactivating convection leads to changes in the simulations: When evaluating experiments with cloud parameterization in both domains against those that deactivate it in d02, the former tend to capture the spatial distribution of precipitation more accurately, showing a less extreme relative bias compared to their counterparts

with explicit resolution in d02. Experiments like Y_KF and Y_GF stand out for their ability to reduce the overestimation or underestimation of precipitation, providing better results in terms of bias and correlation with the observed data. However, with the explicit resolution in both d01 and d02 (Y_OFF), the simulation achieves less underestimation of precipitation throughout the northeast of the study area compared to experiments with parameterizations in both domains. This suggests that allowing the model to resolve convection explicitly could be a valid strategy in a context like the area and event of this study.

- There is no combination of parameterizations that systematically generates the best results across all analyses conducted here. Y_KF_OFF emerges as the best for the 10 mm precipitation threshold. This experiment combines the YSU PBL with the deactivation of cloud parameterization in the inner domain, but with KF in d01. In contrast, for the 1 mm threshold, the best results are obtained with the Y_GD and Y_NT experiments. These demonstrated a perfect detection capability with a low level of false alarms and an excellent ability to capture relevant events. Therefore, Y_KF_OFF is the best experiment for detecting intense precipitation, while Y_GD and Y_NT are more suitable for detecting light rain.

The findings presented here open the door to future research that could further explore the interaction between spatial resolution and the different physical schemes offered by WRF in Peru during El Niño Costero episodes. One important aspect to analyze in the future in depth is the significant impact of the topography on the precipitation simulation. The effects of the extensive complex terrain have been evidenced in the simulations carried out, similarly to other studies in Peru [22,23] and over other complex terrain regions in the world [51], and a tendency to overestimate has been identified over the Andes when a high resolution has been used. It will be interesting in the future to analyze this sensitivity over other kinds of climate conditions like La Niña. Moreover, the authors emphasize that the findings of this study pertain to the spin-up time and model initialization used, and considering the sensitivity to the spin-up conditions will be part of our future work. The sensitivity of a rain forecast depends not only on the PBL and cumulus schemes but also other parameters like initial and boundary conditions or the domain configuration, among others.

Author Contributions: Comceptualization, R.A.A. and M.G.-V.O.; methodology, M.G.-V.O., R.A.A. and A.S.O.; software, A.S.O.; validation, A.S.O.; formal analysis, A.S.O.; investigation, A.S.O.; resources, M.G.-V.O. and R.A.A.; data curation, A.S.O.; writing—original draft preparation, A.S.O.; writing—review and editing, R.A.A. and M.G.-V.O.; visualization, A.S.O.; supervision, M.G.-V.O. and R.A.A.; All authors have read and agreed to the published version of the manuscript.

Funding: M.G.-V.O. was funded by MICIU/AEI/10.13039/501100011033 and by FEDER, UE, in the framework of project PID2021-126401OB-I00.

Data Availability Statement: The raw data supporting the conclusions of this article will be made available by the authors on request.

Conflicts of Interest: The authors declare no conflict of interest.

References

1. Quispe Vega, K.R. El Niño Costero 2017: Precipitaciones Extraordinarias en el Norte de Perú. Master's Thesis, University of Barcelona, Barcelona, Spain, 2018.
2. Hu, Z.Z.; Huang, B.; Zhu, J.; Kumar, A.; McPhaden, M.J. On the variety of coastal El Niño events. *Clim. Dyn.* **2018**, *52*, 7537–7552. [CrossRef]

3. Trenberth, K.E.; Stepaniak, D.P. Indices of el Niño evolution. *J. Clim.* **2001**, *14*, 1697–1701. [CrossRef]
4. Espinoza-Morriberón, D.; Echevin, V.; Colas, F.; Díaz, E.; Tam, J.; Anculle, T.; Ledesma, J.; Gutiérrez, D. Diferencias entre los impactos en la costa peruana de los eventos ENOS cálidos y El Niño Costero 2017: Vientos, afloramiento, productividad y anchoveta. *Bol. Inst. Del Mar Del Perú* **2021**, *36*, 329–348. [CrossRef]
5. Garreaud, R.D.; Vuille, M.; Compagnucci, R.; Marengo, J. Present-day south american climate. *Palaeogeogr. Palaeoclimatol. Palaeoecol.* **2009**, *281*, 180–195. [CrossRef]
6. Takahashi, K.; Montecinos, A.; Goubanova, K.; Dewitte, B. ENSO regimes: Reinterpreting the canonical and Modoki El Niño. *Geophys. Res. Lett.* **2011**, *38*, L10704. [CrossRef]
7. Garreaud, R.D. A plausible atmospheric trigger for the 2017 coastal El Niño. *Int. J. Climatol.* **2018**, *38*, e1296–e1302. [CrossRef]
8. Takahashi, K.; Martínez, A.G. The very strong coastal El Niño in 1925 in the far-eastern Pacific. *Clim. Dyn.* **2019**, *52*, 7389–7415. [CrossRef]
9. Fondo Internacional de Emergencia de las Naciones Unidas para la Infancia. Lluvias e Inundaciones: Fenómeno El Niño–2017. Available online: https://www.unicef.org/peru/emergencias/lluvias-e-inundaciones-fenomeno-el-nino-2017#:~:text=Video%20de%20Sergio%20Ramos%20(Embajador,casas%20y%20fuentes%20de%20ingreso (accessed on 1 December 2024).
10. Macroconsult. Daños de El Niño: US$3,124 millones hasta ahora. 2017. Available online: https://sim.macroconsult.pe/danos-de-el-nino-us3-124-millones-hasta-ahora-macroconsult/ (accessed on 1 December 2024).
11. Díaz, Y.; Díaz, O. *Evaluación del Pronóstico Numérico del Tiempo a Corto Plazo Para Cuba con el Modelo de Mesoescala MM5V3*; Instituto Superior de Tecnologías y Ciencias Aplicadas: Havana, Cuba, 2010.
12. Skamarock, W.C.; Klemp, J.B.; Dudhia, J.; Gill, D.O.; Barker, D.M.; Duda, M.G.; Powers, J.G. A description of the advanced research WRF version 3. *NCAR Tech. Note* **2008**, *475*, 10–5065.
13. Leung, L.R.; Kuo, Y.H.; Tribbia, J. Research needs and directions of regional climate modeling using WRF and CCSM. *Bull. Am. Meteorol. Soc.* **2006**, *87*, 1747–1751. [CrossRef]
14. Bukovsky, M.S.; Karoly, D.J. Precipitation simulations using WRF as a nested regional climate model. *J. Appl. Meteorol. Climatol.* **2009**, *48*, 2152–2159. [CrossRef]
15. Awan, N.K.; Truhetz, H.; Gobiet, A. Parameterization-induced error characteristics of MM5 and WRF operated in climate mode over the Alpine region: An ensemble-based analysis. *J. Clim.* **2011**, *24*, 3107–3123. [CrossRef]
16. González-Rojí, S.J.; Messmer, M.; Raible, C.C.; Stocker, T.F. Sensitivity of precipitation in the highlands and lowlands of Peru to physics parameterization options in WRFV3. 8.1. *Geosci. Model Dev.* **2022**, *15*, 2859–2879. [CrossRef]
17. Müller, O.V.; Lovino, M.A.; Berbery, E.H. Evaluation of WRF model forecasts and their use for hydroclimate monitoring over southern south America. *Weather. Forecast* **2016**, *31*, 1001–1017. [CrossRef]
18. Martínez, J.A.; Arias, P.A.; Castro, C.; Chang, H.I.; Ochoa-Moya, C.A. Sea surface temperature-related response of precipitation in northern South America according to a WRF multi-decadal simulation. *Int. J. Climatol.* **2019**, *39*, 2136–2155. [CrossRef]
19. Back, L.E.; Bretherton, C.S. On the relationship between SST gradients, boundary layer winds, and convergence over the tropical oceans. *J. Clim.* **2009**, *22*, 4182–4196. [CrossRef]
20. Ordoñez Piscoya, J.A. Sensibilidad de la Parametrización de la Convección Utilizando WRF-ARW, Sobre la Sierra Norte del Perú. Master's Theses, Universitat de Barcelona, Barcelona, Spain, 2018.
21. Uribe Cortes, A. Estimación de la Capacidad del Modelo WRF para Pronosticar Eventos Extremos Asociados con Altas Precipitaciones en la Región Andina Colombiana. Master's Thesis, Departamento de Geociencias, Bogota, Colombia, 2012.
22. Mourre, L.; Condom, T.; Junquas, C.; Lebel, T.; ESicart, J.; Figueroa, R.; Cochachin, A. Spatio-temporal assessment of WRF, TRMM and in situ precipitation data in a tropical mountain environment (Cordillera Blanca, Peru). *Hydrol. Earth Syst. Sci.* **2016**, *20*, 125–141. [CrossRef]
23. Moya-Álvarez, A.S.; Martínez-Castro, D.; Kumar, S.; Estevan, R.; Silva, Y. Response of the WRF model to different resolutions in the rainfall forecast over the complex Peruvian orography. *Theor. Appl. Climatol.* **2019**, *137*, 2993–3007. [CrossRef]
24. Zhang, C.; Wang, Y.; Hamilton, K. Improved representation of boundary layer clouds over the southeast Pacific in ARW-WRF using a modified Tiedtke cumulus parameterization scheme. *Mon. Weather Rev.* **2011**, *139*, 3489–3513. [CrossRef]
25. ENFEN. 2017. Informe Técnico ENFEN Nº 4. Abril 2017. Available online: https://www.dhn.mil.pe/Archivos/oceanografia/enfen/informe-tecnico/04-2017.pdf (accessed on 1 December 2024).
26. Neyra Celi, D.A.; Olivares Castillo, A. *Análisis Hidrometeorológico de la Cuenca del río Piura Durante El Niño Costero 2017*; University of Piura: Piura, Peru, 2019.
27. Funk, C.; Peterson, P.; Landsfeld, M.; Pedreros, D.; Verdin, J.; Shukla, S.; Husak, G.; Rowland, J.; Harrison, L.; Hoell, A.; et al. The climate hazards infrared precipitation with stations—A new environmental record for monitoring extremes. *Sci. Data* **2015**, *2*, 150066. [CrossRef] [PubMed]

28. Hersbach, H.; Bell, B.; Berrisford, P.; Hirahara, S.; Horányi, A.; Muñoz-Sabater, J.; Nicolas, J.; Peubey, C.; Radu, R.; Schepers, D.; et al. The ERA5 global reanalysis. *Q. J. R. Meteorol. Soc.* **2020**, *146*, 1999–2049. [CrossRef]
29. Balmaceda Huarte, R.; Olmo, M.E.; Bettolli, M.L.; Poggi, M.M. Evaluation of multiple reanalyses in reproducing the spatio-temporal variability of temperature and precipitation indices over southern South America. *Int. J. Climatol.* **2021**, *41*, 5572–5595. [CrossRef]
30. Hassler, B.; Lauer, A. Comparison of reanalysis and observational precipitation datasets including ERA5 and WFDE5. *Atmosphere* **2021**, *12*, 1462. [CrossRef]
31. Givati, A.; Lynn, B.; Liu, Y.; Rimmer, A. Using the WRF Model in an Operational Streamflow Forecast System for the Jordan River. *J. Appl. Meteorol. Clim.* **2012**, *51*, 285–299. [CrossRef]
32. Tian, J.; Liu, J.; Yan, D.; Li, C.; Yu, F. Numerical rainfall simulation with different spatial and temporal evenness by using a WRF multiphysics ensemble. *Nat. Hazards Earth Syst. Sci.* **2017**, *17*, 563–579. [CrossRef]
33. Hu, X.M.; Nielsengammon, J.W.; Zhang, F. Evaluation of three planetary boundary layer schemes in the WRF model. *J. Appl. Meteorol. Clim.* **2010**, *49*, 1831–1844. [CrossRef]
34. Deng, C.; Chi, Y.; Huang, Y.; Jiang, C.; Su, L.; Lin, H.; Jiang, L.; Guan, X.; Gao, L. Sensitivity of WRF multiple parameterization schemes to extreme precipitation event over the Poyang Lake Basin of China. *Front. Environ. Sci.* **2023**, *10*, 1102864. [CrossRef]
35. Hiraga, Y.; Tahara, R. Sensitivity of localized heavy rainfall in Northern Japan to WRF physics paameterization schemes. *Atmos. Res.* **2024**, *314*, 108802. [CrossRef]
36. Liu, Y.; Zhuo, L.; Han, D. Developing spin-up time framework for WRF extreme precipitation simulations. *J. Hydrol.* **2023**, *620*, 129443. [CrossRef]
37. Wang, S.; Yu, E.; Wang, H. A simulation study of a heavy rainfall process the Yangtze River valley using the two-way nesting approach. *Adv. Atmos. Sci.* **2012**, *29*, 731–743. [CrossRef]
38. Niu, G.Y.; Yang, Z.L.; Mitchell, K.E.; Chen, F.; Ek, M.B.; Barlage, M.; Kumar, A.; Manning, K.; Niyogi, D.; Rosero, E.; et al. The community Noah land surface model with multiparameterization options (Noah-MP): 1. Model description and evaluation with local-scale measurements. *J. Geophys. Res. Atmos.* **2011**, *116*. [CrossRef]
39. Da Silva, L.F.C.; Getirana, A.; Filho OC, R.; Gustavo, L.; de Goncalves, G. Balanço hídrico e eventos extremos na américa do sul mediante acoplamento entre modelo de escoamento hymap e modelos de superfície noah-mp e clsm. In Proceedings of the XXIII Simpósio Brasileiro de Recursos Hídricos, Foz do Iguaçu, Brazil, 24–28 November 2019.
40. Schulzweida, U.; Kornblueh, L.; Quast, R. CDO User Guide; 2019; Available online: https://users.rcc.uchicago.edu/~davidkelly999/cdo.pdf (accessed on 1 December 2024).
41. Ebert, E.E. Fuzzy verification of high-resolution gridded forecasts: A review and proposed framework. *Meteorol. Appl. A J. Forecast. Pract. Appl. Train. Tech. Model.* **2008**, *15*, 51–64. [CrossRef]
42. Rojas, N.; Rojas, J. Análisis y simulación de los procesos atmosféricos e hidrológicos usando el modelo atmosférico WRF en el Perú durante el 2014. *Rev. Investig. Física* **2020**, *23*, 43–48. [CrossRef]
43. Shin, H.H.; Hong, S.Y. Intercomparison of planetary boundary-layer parametrizations in the WRF model for a single day from CASES-99. *Bound. Layer Meteorol.* **2011**, *139*, 261–281. [CrossRef]
44. Moya-Álvarez, A.S.; Martínez-Castro, D.; Flores, J.L.; Silva, Y. Sensitivity study on the influence of parameterization schemes in WRF_ARW model on short-and medium-range precipitation forecasts in the Central Andes of Peru. *Adv. Meteorol.* **2018**, *2018*, 1381092. [CrossRef]
45. Solano-Farias, F.; Ojeda MG, V.; Donaire-Montaño, D.; Rosa-Cánovas, J.J.; Castro-Díez, Y.; Esteban-Parra, M.J.; Gámiz-Fortis, S.R. Assessment of physical schemes for WRF model in convection-permitting mode over southern Iberian Peninsula. *Atmos. Res.* **2024**, *299*, 107175. [CrossRef]
46. Han, J.Y.; Hong, S.Y. Precipitation forecast experiments using the Weather Research and Forecasting (WRF) Model at gray-zone resolutions. *Weather. Forecast.* **2018**, *33*, 1605–1616. [CrossRef]
47. Alsilibe, F.; Bene, K.; Bilal, G.; Alghafli, K.; Shi, X. Accuracy assessment and validation of multi-source CHIRPS precipitation estimates for water resource management in the Barada Basin, Syria. *Remote Sens.* **2023**, *15*, 1778. [CrossRef]
48. Prein, A.F.; Gobiet, A.; Truhetz, H.; Keuler, K.; Goergen, K.; Teichmann, C.; Fox Maule, C.; van Meijgaard, E.; Déqué, M.; Nikulin, G. Precipitation in the EURO-CORDEX 0.11° and 0.44° simulations: High resolution, high benefits? *Clim. Dyn.* **2016**, *46*, 383–412. [CrossRef]
49. Pastor, F.; Gómez, I.; Estrela, M.J. Numerical study of the October 2007 flash flood in the Valencia region (Eastern Spain): The role of orography. *Nat. Hazards Earth Syst. Sci.* **2010**, *10*, 1331–1345. [CrossRef]

50. Jeworrek, J.; West, G.; Stull, R. Evaluation of cumulus and microphysics parameterizations in WRF across the convective grey zone. *Weather Forecast.* **2019**, *34*, 1097–1115. [CrossRef]
51. Li, J.; Lu, C.; Chen, J.; Zhou, X.; Yang, K.; Li, J.; Wu, X.; Xu, X.; Wu, S.; Hu, R.; et al. The influence of complex terrain on cloud and precipitation on the foot and slope of the southeastern Tibetan Plateau. *Clim. Dyn.* **2024**, *62*, 3143–3163. [CrossRef]